Magnetic properties of iron oxide nanoflowers

Author: Iker García González
Facultat de Física, Universitat de Barcelona, Diagonal 645, 08028 Barcelona, Spain

Advisor: Amílcar Labarta Rodríguez
(Dated: January 19, 2022)

Abstract: Maghemite multi-core nanoparticles have been modelled to better understand their magnetic properties and the collective interactions from where they arise. Micromagnetic simulations with different values of the relevant parameters have been performed to reproduce the experimental results. The role of the exchange interaction between cores is studied. An analysis of the resulting magnetisation hysteresis loops is done, as well as the vorticity and topological properties of the magnetisation configuration.

I. INTRODUCTION

Multi-core iron oxide nanoparticles, such as nanoflowers (NF), have been thoroughly investigated in the last years due to their promising applications. In biomedicine, their size is comparable or smaller than cells [1], and hence can interact with them. They can be used for magnetic hyperthermia [2] when applying an alternating magnetic field, or drug delivery [3] when coated with a drug. They can also be used for non medical applications, such as water remediation [4]. One of the properties that make these applications possible is that they are relatively big nanoparticles, which yields a high saturation magnetisation. Moreover, they have a very low remanence despite their size compared to single-core nanoparticles or bulk materials. This leads to the fact that they do not form aggregates in a colloidal suspension. They have a very big initial magnetic susceptibility and can be saturated with a relatively low applied magnetic field. In order to optimise these properties for their applications, knowledge of the interactions between cores and the magnetic variables at play is needed.

This work will focus on maghemite (γFe_2O_3) NFs, and we will call each core a nanopetal (NP) to maintain the metaphor. Maghemite has a cubic crystalline structure and is ferrimagnetic in bulk. Some experimental results from a typical NF sample are shown in Fig. 1, extracted from [5]. A high resolution transmission electronic microscopy (HRTEM) image of a NF is shown in Fig. 1a. HRTEM images and micro-diffraction experiments (see Fig. 1b) show that there is an important level of crystalline correlation among NPs, known as crystalline texture. That is, the crystal axes of each NP are correlated to the rest of the NPs, and have a deviation of around 10° from each other, as shown by the small arcs in the diffraction pattern. This crystalline correlation among the cores produces a certain magnetic interaction among NPs, which is important for the magnetic configuration. These particles are not uniform in size, but the size distribution is relatively narrow as shown in Fig. 1c. An experimental hysteresis loop for these samples is also shown in Fig. 1d, which exhibits the aforementioned magnetic properties. Our aim is to reproduce the main magnetic properties using the experimental knowledge of the NFs.

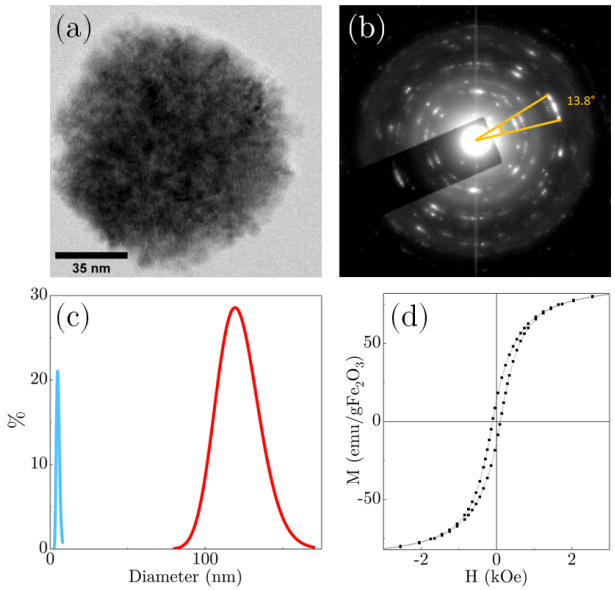

FIG. 1: (a) HRTEM image of a NF. (b) Micro-diffraction pattern showing the crystalline texture of the NPs within the NF. (c) Size distribution of the NFs (red) and the NPs (blue). (d) Experimental hysteresis loop at $T = 5$ K.

II. MICROMAGNETIC APPROXIMATION

Micromagnetics (MM) is a quasi-classical theory developed to describe phenomena in the nanometer to micrometer scale [6], where it is not necessary to carry out detailed atomistic calculations to account for the magnetic properties of materials. At the micrometer scale, simulations using quantum theory are not computationally efficient, and they can only be used for systems on the nanometer scale. On the contrary, classical models do not reproduce the desired physical properties which are relevant at the micrometer scale.

In micromagnetism, it is assumed that the local magnetisation vector $\vec{M}(\vec{r})$ is a continuous function in space. It replaces the discrete atomic spins with mesoscopic size elements, whose magnetisation can be treated with a semi-classical Hamiltonian. The magnetisation has a constant magnitude $|\vec{M}| = M_s$, the saturation magneti-

sation, and can only rotate. Hence, we can consider the magnetisation unit vector $\vec{m} = \vec{M}/M_s$.

There are a few energy terms that come into play in MM, and in particular in our system. The exchange energy between two spins is given by the Heisenberg Hamiltonian. After considering the MM framework and integrating in a volume V, it becomes

$$E_{ex} = \int_V A\left((\nabla m_x)^2 + (\nabla m_y)^2 + (\nabla m_z)^2\right) dV, \quad (1)$$

where A is the exchange constant (EC) which depends on the material and its crystal structure. In NFs, we will have two ECs, one between points in the same NP, A_w, and a smaller one between points in neighbouring NPs, A_i.

If $\vec{\mu}$ is a magnetic dipole, its energy in an external magnetic field $\vec{H}$ is $E = \vec{\mu} \cdot \vec{H}$. In the continuum, we can integrate over the volume to get its Zeeman energy:

$$E_Z = -\mu_0 M_s \int_V \vec{m} \cdot \vec{H} dV. \quad (2)$$

In the crystal, every dipole is exposed to the field created by the other dipoles. Considering the magnetic field created by a dipole and integrating over approximately the whole volume, the demagnetising field at each point is

$$\vec{H}_{demag}(\vec{r}) = \frac{M_s}{4\pi} \int_V \Big(3\frac{[\vec{m}(\vec{r}') \cdot (\vec{r} - \vec{r}')](\vec{r} - \vec{r}')}{|\vec{r} - \vec{r}'|^5} - \frac{\vec{m}(\vec{r}')}{|\vec{r} - \vec{r}'|^3}\Big) dV. \quad (3)$$

Thus, the total energy due to the demagnetisation is

$$E_{demag} = -\frac{\mu_0 M_s}{2} \int_V \vec{m} \cdot \vec{H}_{demag} dV, \quad (4)$$

where the $1/2$ factor appears to count each pair of dipoles only once.

The axes in the cubic crystalline structure of maghemite introduce anisotropies, which are intrinsic to the material. If $\vec{u}_1, \vec{u}_2, \vec{u}_3$ are the cubic anisotropy (CA) axes, the CA energy can be calculated as

$$E_{CA} = K_c \int_V \sum_{j \neq k} (\vec{m} \cdot \vec{u}_j)^2 (\vec{m} \cdot \vec{u}_k)^2 dV. \quad (5)$$

The shape and the surface of each NP produces an effective uniaxial anisotropy (UA) which has a random direction for each NP. Its energy can be calculated as

$$E_{UA} = -K_u \int_V (\vec{m} \cdot \vec{u})^2 dV, \quad (6)$$

where $\vec{u}$ is the anisotropy axis. The total energy is

$$E_{tot} = E_{ex} + E_Z + E_{demag} + E_{UA} + E_{CA}, \quad (7)$$

and the magnetisation configuration results from minimising this energy. This energy can be considered as a result of an effective magnetic field

$$\vec{H}_{eff} = -\frac{1}{\mu_0 M_s} \frac{\delta E_{tot}}{\delta \vec{m}}. \quad (8)$$

The dynamics of the magnetisation processes are governed by the Landau–Lifshitz–Gilbert (LLG) equation

$$\frac{\partial \vec{m}}{\partial t} = -\gamma \mu_0 \vec{m} \times \vec{H}_{eff} + \alpha \vec{m} \times \frac{\partial \vec{m}}{\partial t}, \quad (9)$$

where γ and α are constants. The first term in the right-hand side represents the precession of the magnetisation produced by the magnetic torque, and the second one is a damping term, which directs the magnetisation towards the effective field.

Solving the LLG equation analytically is impossible for complex systems, thus different simulation environments have been built to solve it numerically. OOMMF (Object Oriented MicroMagnetic Framework) [7] is the software used in this paper, which uses a finite differences method to solve LLG. A regular rectangular grid divides the space into a discrete mesh with spacing h. The size of the mesh has to be smaller than the magnetostatic exchange length [6],

$$\ell_{ex} = \sqrt{\frac{2A}{\mu_0 M_s^2}}. \quad (10)$$

Roughly, it is the length scale at which the exchange energy is a relevant term compared to the magnetostatic energy, hence, the range of the exchange interaction between points in the mesh. The magnetisation is evaluated at the center points of the mesh, and all the energy terms in Eq. (7) are calculated using discrete approximations.

III. SYSTEM AND MICROMAGNETIC SIMULATIONS

The approximation of the real system is done by building a sphere with cubes, as shown in Fig. 2, where each cube represents a different petal in the NF. The sphere has a diameter of 160 nm and each cube has a side length of 16 nm, where a cube is part of the sphere if its center is at a distance smaller than 80 nm from the center of the sphere. We will use a mesh size of $h = 4$ nm,

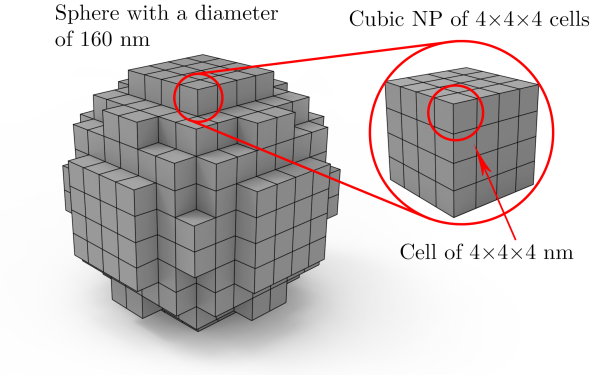

FIG. 2: System set up

which allows greater detail in the magnetisation configuration and to assign different properties to the surface of each NP and its inside. A different pairwise EC is used for cells belonging to the same or different cubes, which mimics the weaker interaction between NPs in the real NF. The EC is $A_w = 7 \times 10^{-12}$ J/m [8] for neighbouring cells within the same NP, and for neighbouring cells in different cubes it will be a percentage of that value. The saturation magnetisation for maghemite is $M_s = 4.8{\times}10^5$ A/m [8]. Hence, the value of h is smaller or, at most, the same order of magnitude as ℓ_{ex} in Eq. (10) using the previous parameters. This validates the use of the MM framework.

Each NP has a slightly different shape, thus each one of them has a different UA axis. The axis for the UA for each NP is defined via an external file, which is in turn created using a custom `C++` script which generates uniformly randomly oriented unit vectors. For the CA, two vectors are generated using a `C++` script. Given that the NPs present an important crystalline texture, one vector has a normal distribution around the z axis with a standard deviation of 5°, and the other is perpendicular to it with a uniform distribution of orientations. The values for the CA and UA constants for maghemite are $K_c = -1.3 \times 10^4$ J/m^3 [8] and $K_u = -5 \times 10^3$ J/m^3, respectively, where the UA constant is a reasonable value for particles of this size. Also, a simulated temperature is used. This is not a real temperature, since MM does not account for it, but an approximation to introduce noise and reduce the possibility of the system getting stuck in local minima. After some tests, the value of $T = 10$ K was decided as a balance between noise and detail. A variation of a simple first order Euler method will be used to solve Eq. (9), which accounts for this temperature.

IV. SIMULATION RESULTS

Our aim is to study the changes in the local magnetisation when a magnetic field is applied in the z direction. This external field is applied following discrete time steps, and various convergence criteria can be used to decide when to initiate the next step. A common criterion is an upper bound on $|d\vec{m}/dt|$, but when using it at $T = 0\,\mathrm{K}$, the system gets stuck in metastable states yielding non-physical hysteresis loops, like crossings between the paths (see Fig. 3a). When adding a non-zero temperature, criteria based on the convergence of $|d\vec{m}/dt|$ were discarded as the fluctuations in the magnetisation were greater than any reasonable upper bound for $|d\vec{m}/dt|$. Hence, time criteria were used. Given that the path of a hysteresis loop follows metastable states, the results depend on the observation time and the steps taken when varying the applied field. Thus, different stopping times were used, as shown in Fig. 3, for a total number of 320 field steps. The bigger the stopping time, the more detail shown in the hysteresis loop, but also the longer total simulation run time. Hence, a stopping time of $5 \times 10^{-9}\,\mathrm{s}$ will be used for the following simulations, which is a compromise for both factors.

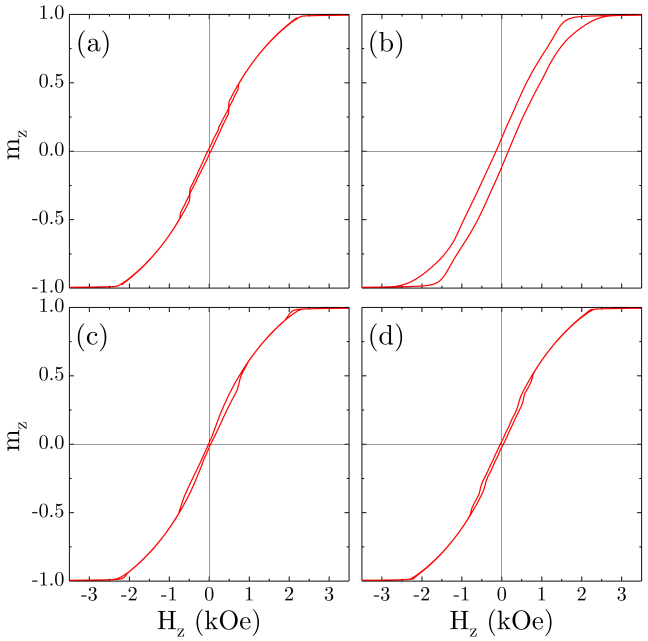

FIG. 3: Hysteresis loop (a) without temperature for $|d\vec{m}/dt| < 0.5$ ns^{-1}; and with $T = 10$ K for stopping time of (b) $5 \cdot 10^{-11}$ s, (c) $5 \cdot 10^{-10}$ s and (d) $5 \cdot 10^{-9}$ s.

One of the unknown parameters in a NF is the interaction between NPs, so various simulations were done varying the EC between cells in neighbouring petals A_i, namely 1%, 10%, 50%, and 100% of A_w. The results are presented in Fig. 4. The hysteresis loops become more square-like, have bigger jumps as well as bigger remanence and coercivity with an increasing EC. This behaviour is expected since, when increasing the A_i, the NF becomes more ferrimagnetic overall and the magnetic correlation within the system increases.

An important remark is that the same random anisotropies were used in all the simulations, and hence, the results are dependent on the particular realization of the system. Thus, the detail in the non-reversible part in the hysteresis loops in Fig. 4 is the result of this particular configuration of anisotropies. Nevertheless, some preliminary simulations with other random anisotropies yield similar global behaviour.

At a low magnetic field, a vortex-like arrangement of the magnetisation is found. This is due to the effect of the demagnetising field [9] and the low interaction between NPs. This type of complex structure is what gives the system its low remanence and coercivity, and it is overridden as a stronger field is applied, since the magnetisation tends to align along it. Various stages of the vortex structure are shown in Fig. 5. The first snapshot (Fig. 5a) shows the system with no field applied (remnant state), after magnetic saturation in the positive direction. At this stage, there is little remanence in

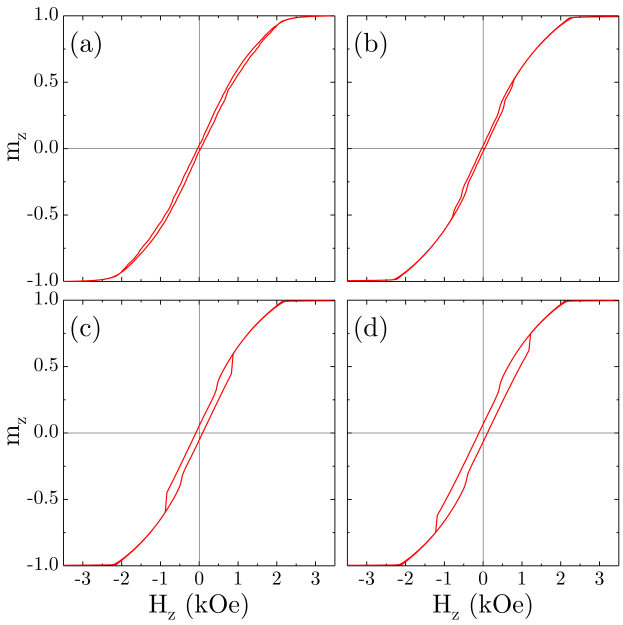

FIG. 4: Hysteresis loop for inter-petal EC of (a) 1%, (b) 10%, (c) 50% and (d) 100% of A_w.

the magnetisation due to the vortex configuration. The second one (Fig. 5b) is at $H_z = -1.269$ kOe after 5a. Notice the inversion in the spin direction of the magnetisation between Fig. 5b and Fig. 5c after saturation. Also note that the magnetisation near the center of the vortex tends to align with the magnetic field and even goes out of plane at remanence, conferring a certain polarity to the vortex.

V. VORTICITY AND TOPOLOGICAL NUMBER

One can define the vorticity $\vec{v}$ of the magnetisation as its curl $\vec{v} = \vec{\nabla} \times \vec{m}$. Since the magnetisation is a discrete field, a discrete approximation is taken when calculating the vorticity. Plotting the average z component of the vorticity against the applied field, we can get an idea of the vorticity at each field step (Fig. 6). One can see that the sudden changes in magnetisation are highly correlated with changes in the vorticity, as these changes are the result of reconfigurations of the magnetisation. Also, one can see that the chirality of the vortex is reversed when the system is saturated and then desaturated. When the system is at saturation, there is no vorticity, and when the applied field is reduced, the vortex starts to form in the chirality that lowers the energy according to the random anisotropies present in the system, which is at opposite directions whether the applied field is positive or negative. At low magnetic fields, the vorticity is lower than expected because at this point the anisotropies have a more dominant effect in the system, and thus the magnetisation does not align with a perfect vortex. In particular, the jumps seen in Fig. 6a between $H_z = \pm 0.8$ kOe are the result of the specific anisotropies used in this simulation and are expected to change should another configuration be used. In Fig. 6b, one can see that this effect is increased with a lower A_i, since there is less correlation between neighbouring NPs and more disturbances in the vortex arrangement are expected. There may even be domains in which the magnetisation does not align with the rest. With bigger A_i, there is a greater vorticity and the effects of the anisotropies are reduced.

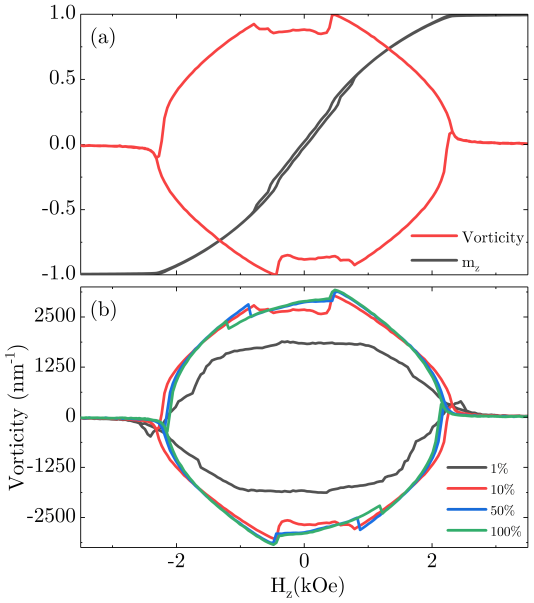

FIG. 6: (a) Normalised vorticity and normalised magnetisation for different applied fields for the case $A_i = 0.1A_w$. (b) Vorticity for the different A_i.

Another point of view from which we can study the magnetisation configuration is topology, which lets us classify these types of vortex structures. The magnetisation $\vec{m}(\vec{r})$ is a unit vector, and so it can be viewed as a point on the sphere S^2. Hence we can map a cross section to the sphere via the stereographic projection, and in turn, we can think of $\vec{m}(\vec{r})$ as a mapping from the sphere to the sphere. This lets us use the following fact derived from algebraic topology: the mappings from the sphere to the sphere can be classified according to how many times it "wraps" around itself [10], which is analogous to the winding number for curves in the plane. In our case, we can classify magnetisation configurations according to this number, which we will call W. One can derive [11] that

$$W = \frac{1}{4\pi} \iint \vec{m} \cdot \left(\frac{\partial \vec{m}}{\partial x} \times \frac{\partial \vec{m}}{\partial y} \right) dxdy. \qquad (11)$$

Calculating W for each step in the $z = 0$ cross section, we can plot its hysteresis loop. The case for $A_i = 0.1A_w$ is plotted in Fig. 7. Note that the changes in W are also correlated with the changes in the magnetisation, and there is only a non-zero value in the non-reversible parts

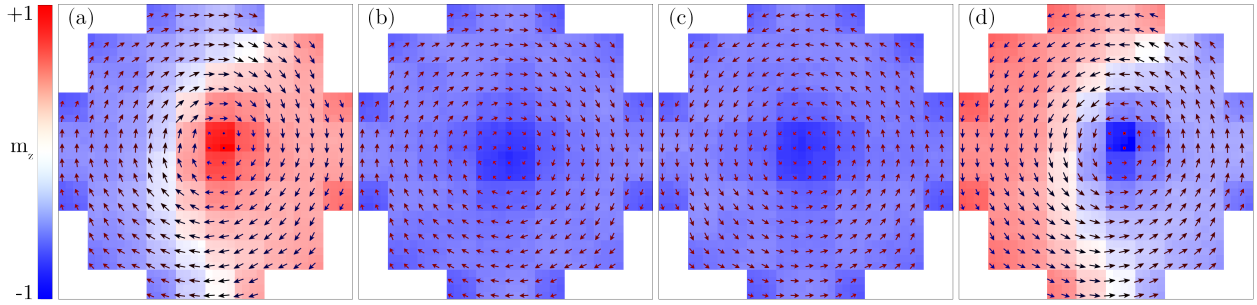

FIG. 5: Magnetisation field in the $z = 0$ plane for different applied fields and $A_i = 0.1A_w$. The cell colour represents the sign of the m_z component, and the arrow colour is the inverse colour map. (a) $H_z = 0$ kOe, (b) $H_z = -1.269$ kOe, (c) $H_z = -1.269$ kOe, (d) $H_z = 0$ kOe.

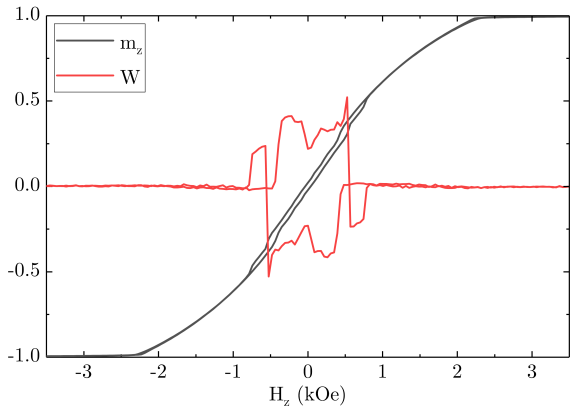

FIG. 7: Topological number W and normalised magnetisation as a function of H_z.

of the hysteresis loop. The value of W and its behaviour with respect to the applied field varies greatly depending on the value of A_i. Its maximum value is attained for $A_i = 0.1A_w$, and the maximum values for the rest of the studied A_i are less than 0.2. This means that the most stable magnetic structure from the topological point of view is for $A_i = 0.1A_w$.

Notice from Eq. (11) that W is a product of two numbers, the magnetisation direction and the magnetisation winding number. The jump from a negative to a positive W in Fig. 7 at $H_z = \pm 0.55$ kOe is explained by this product, since the magnetisation around the central axis changes sign at this point.

It is worth noting that W does not attain an integer value, and its maximum value is around 0.5. Hence, there is no protected topological structure created like a skyrmion for any value of the applied field.

VI. CONCLUSIONS

We have been able to reproduce the main phenomenology of the phyiscal system and simulate a hysteresis loop similar to the experimental data. We have shown that the magnetic exchange between NPs is a relevant parameter explaining the behaviour of the NFs. We have also shown that the vorticity produced by the demagnetising field causes the low remanence, and we have studied its changes with the applied field. Lastly, the winding number can reach high values in some cases, which may explain the certain stability of the vortex configuration.

Acknowledgments

Thanks to my advisor, Amílcar Labarta, for his patience, knowledge and guidance, as well as Javier Rodríguez for his advice and problem-solving skills. This work would not be possible without them. Thanks to Josep Rius for his help with OOMMF, and Adrián Natal for the render in Fig. 2. Thanks to my parents and sister for their support during these years. And last, but definitely not least, thanks to my friends and colleagues.

[1] A. Kostopoulou and A. Lappas, Nanotechnology Rev. **4**, 595-624 (2015).
[2] L. Storozhuk et al., ACS Appl. Mater. Inter. **13**, 45870-45880 (2021).
[3] E. Amstad, M. Textor, and E. Reimhult, Nanoscale **3**, 2819 (2011).
[4] A. Gallo-Cordova et al., J. Cleaner Production **308**, 127385 (2021).
[5] M. Escoda i Torroella, *Tuning the performance of magnetic, semiconductor, and multifunctional hybrid nanostructures*, PhD thesis, Universitat de Barcelona (2022).
[6] L. Exl, D. Suess, and T. Schrefl *Micromagnetism.* In: J. M. D. Coey and S. Parkin (eds.) *Handbook of Magnetism and Magnetic Materials*. Springer International Publishing (2020).
[7] M. J. Donahue and D. G. Porter, *OOMMF User's Guide*, NIST (2020).
[8] J. M. D. Coey, *Magnetism and Magnetic Materials*, Cambridge University Press (2010).
[9] X. Zhang, Y. Zhou, and M. Ezawa, Phys. Rev. B **93**, 024415 (2016).
[10] The second homotopy group of the sphere is isomorphic to the integers, that is $\pi_2(S^2) \equiv \mathbb{Z}$.
[11] H.-B. Braun, Adv. Phys. **61**, 1 (2012).